

Tensor description of X-ray magnetic dichroism at the Fe $L_{2,3}$ -edges of Fe_3O_4

Hebatalla Elnaggar,^{a*} Maurits W. Haverkort,^b Mai Hussein Hamed,^{c,d} Sarnjeet S. Dhesi^e and Frank M. F. de Groot^{a*}

^aDebye Institute for Nanomaterials Science, Utrecht University, 99 Universiteitsweg, Utrecht 3584 CG, The Netherlands, ^bInstitute of Theoretical Physics, Heidelberg University, 19 Philosophenweg, Heidelberg 69120, Germany, ^cJülich Centre for Neutron Science, Forschungszentrum Jülich GmbH, Jülich 52425, Germany, ^dFaculty of Science, Helwan University, Cairo 11795, Egypt, and ^eDiamond Light Source, Harwell Science and Innovation Campus, Didcot OX11 0DE, United Kingdom. *Correspondence e-mail: h.m.e.a.elnaggar@uu.nl, f.m.f.degroot@uu.nl

Received 1 September 2020

Accepted 11 November 2020

Edited by K. Kvashnina, ESRF – The European Synchrotron, France

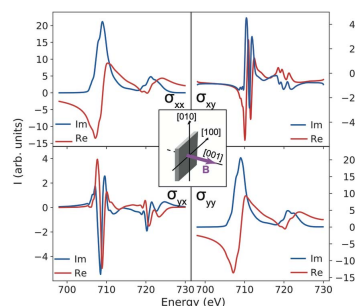
Keywords: X-ray absorption spectroscopy; magnetic dichroism; fundamental spectra; tensor analysis.

A procedure to build the optical conductivity tensor that describes the full magneto-optical response of the system from experimental measurements is presented. Applied to the Fe $L_{2,3}$ -edge of a 38.85 nm $\text{Fe}_3\text{O}_4/\text{SrTiO}_3$ (001) thin-film, it is shown that the computed polarization dependence using the conductivity tensor is in excellent agreement with that experimentally measured. Furthermore, the magnetic field angular dependence is discussed using a set of fundamental spectra expanded on spherical harmonics. It is shown that the convergence of this expansion depends on the details of the ground state of the system in question and in particular on the valence-state spin-orbit coupling. While a cubic expansion up to the third order explains the angular-dependent X-ray magnetic linear dichroism of Fe^{3+} well, higher-order terms are required for Fe^{2+} when the orbital moment is not quenched.

1. Introduction

The determination of the electronic and magnetic structure of engineered magnetic nanostructures is essential to tailor their properties for technological applications such as information storage, spin transport and sensing technology. These devices often rely on magnetic thin-films and nanostructures comprising multiple layers, such as for instance transition metal-oxides magnetic tunnel junctions and exchange biased systems. X-ray magnetic dichroism spectroscopy is a powerful tool that can provide element- and site-specific magnetic information in heteromagnetic nanostructures (Kuiper *et al.*, 1993; Nunez Regueiro *et al.*, 1995; Alders *et al.*, 1998; Scholl *et al.*, 2000; Hillebrecht *et al.*, 2001; Haverkort *et al.*, 2004; van der Laan, 2013; Luo *et al.*, 2019). X-ray magnetic circular dichroism (XMCD) can be used to determine the spin and orbital magnetic moments using sum rules (Carra *et al.*, 1993) while X-ray magnetic linear dichroism (XMLD) can be used to determine the site symmetry, anisotropic magnetic moments and spin-orbit interaction (Lüning *et al.*, 2003; Csiszar *et al.*, 2005; Arenholz *et al.*, 2006; Finazzi *et al.*, 2006; van der Laan *et al.*, 2011; Chen *et al.*, 1992, 2010; Iga *et al.*, 2004). However, using dichroism experiments for magnetometry is far from being straightforward because it requires an understanding of the spectral shape and magnitude of the dichroism signal as well as its dependence on the relative orientation of the X-ray polarization, the exchange field and the crystallographic axes.

The aim of this work is to provide a general method to construct and analyse dichroism effects in dipole transitions such as at the Fe $L_{2,3}$ -edge in magnetite (Fe_3O_4). We illustrate



the procedure to build the conductivity tensor from a few well chosen experimental measurements describing all possible dichroism effects at a single magnetic field orientation. Furthermore, the angular dependence of the magnetic field is discussed using a set of fundamental spectra expanded using spherical harmonics which can describe the full magneto-optical response of the system (Haverkort *et al.*, 2010). Such expansions have been used previously to explain the angular dependence of XMLD (Arenholz *et al.*, 2006, 2007; van der Laan *et al.*, 2008, 2011), yet the new aspect we provide in this work is a thorough inspection of the convergence of the expansion using a comprehensive set of XMLD data measured on Fe₃O₄ in combination with theoretical calculations. Fe₃O₄ serves as an adequate model system: it is a ferrimagnetic mixed-valence strongly correlated system containing two different Fe sites where Fe³⁺ ions reside in tetrahedral (*T_d*) coordinated intersites (*A* sites), while both Fe²⁺ and Fe³⁺ ions are in octahedral (*O_h*) coordinated intersites (*B* sites). This provides us with an opportunity to study the effect of the electronic structure on the quality of the expansion between the orbital singlet Fe³⁺ and the orbital triplet Fe²⁺ ions.

2. Methods

2.1. Experimental

The Fe₃O₄ thin-film was grown on a conductive 0.1% Nb-doped SrTiO₃ (001) TiO₂-terminated substrate using pulsed laser deposition as reported by Hamed *et al.* (2019). The film thickness and surface roughness were concluded to be 38.85 nm and 0.4 nm, respectively, from X-ray reflectivity measurements (Fig. 10 of Appendix A). The Verwey transition was observed at 114.97 ± 0.29 K from the magnetization versus temperature measurements in zero field cooling mode with 500 Oe applied field (Fig. 11 of Appendix A). Hysteresis measurements were also performed along the [1,0,0] direction to inspect the saturation of the thin-film below and above the Verwey transition (Fig. 11 of Appendix A). The largest coercivity is observed for the lowest temperature (*H_c* = 0.1 T) and an external magnetic field of ~0.25 T is required to saturate the in-plane magnetization (see Fig. 12 of Appendix A). On the contrary, the magnetization is not saturated along the [0,0,1] direction with a field of *H* = 2 T as shown by the XMCD measurement shown in (Fig. 13 of Appendix A).

X-ray absorption spectroscopy (XAS) measurements were carried out on beamline I06 of Diamond Light Source, UK. The beam spot at the sample position was estimated to be ~200 μm × 100 μm. The polarization of the beam can be controlled using an Apple-II type undulator to produce linearly and circularly polarized X-rays. A vector magnet set to 1 T was used to saturate the magnetization to (nearly) any arbitrary direction. All measurements were performed at *T* = 200 K in a normal-incidence configuration, *i.e.* with the incoming beam impinging at an angle of 90° with respect to the sample surface. The energy resolution was estimated to be ~200 meV full width at half-maximum (FWHM). The measurements were performed in total electron yield mode. All experimental spectra were first normalized to the incident

photon flux. The spectra were then fitted using a model consisting of two error functions to take into account the *L*_{2,3}-edge jumps. In addition, a set of Gaussian functions were used to fit the multiplet features of the spectra (refer to Appendix B for more details). The *L*_{2,3}-edge jumps were subtracted from the spectra and the spectra were renormalized to the spectral area.

2.2. Computational

The data treatment and the Kramers–Kronig transformation were performed using Python. Crystal field multiplet calculations were performed using the quantum many-body program *Quanty* (Haverkort *et al.*, 2012). The Hamiltonian we use is of the form

$$H = H_{e-e} + H_{SO} + H_{CF} + H_{exch}. \quad (1)$$

The electron–electron Hamiltonian (*H_{e-e}*) is of the form

$$H_{e-e} = \sum_k f_k F^k + \sum_k g_k G^k, \quad (2)$$

where *F^k* (*f_k*) and *G^k* (*g_k*) are the Slater–Condon parameter for the radial (angular operators) part of the direct and exchange Coulomb interactions, respectively. The radial integrals are obtained from atomic Hartree–Fock calculation scaled to 70% and 80% for valence and valence-core interactions, respectively, to take into account interatomic screening and mixing effects. This is in line with works in the literature such as those by Arenholz *et al.* (2006) and Patrick *et al.* (2002). This reduction is related to two effects: (i) the 80% reduction is to correct the Hartree–Fock calculations such that they agree with atomic data, as shown by Cowan (1981) and many others; (ii) the additional reduction to 70% is to take into account the effects of charge transfer; in other words, the nephelauxetic effects.

The spin–orbit Hamiltonian (*H_{SO}*) is of the form

$$H_{SO} = \xi \sum_i l_i \cdot s_i, \quad (3)$$

where *l_i* and *s_i* are the one electron orbital and spin operators, respectively, and the sum over *i* is over all electrons. The prefactor *ξ* is an atom-dependent constant (which is to a good approximation material independent) and hence we used here tabulated data for this with *ξ* = 0.052 eV for 3*d* orbitals and *ξ* = 8.20 eV for 2*p* orbitals.

The crystal field Hamiltonian (*H_{CF}*) is of the form

$$H_{CF} = \sum_{k=0}^4 \sum_{m=-k}^k A_{k,m} C_{k,m}(\theta, \phi), \quad (4)$$

where *C_{k,m}*(*θ, φ*) are the angular crystal field operators expanded on renormalized spherical harmonics and *A_{k,m}* are proportional to the distortion parameters used in crystal field theory, 10*D_q*, *D_s* and *D_t*. In cubic symmetry we consider only 10*D_q* which we found to be 1.25 eV and 0.5 eV for the *B* and *A* sites, respectively, by fitting to the XAS and XMCD spectra. The optimized parameters used for the calculations can be found in Tables 4, 5 and 6. Details of the ground state for the three Fe ions in Fe₃O₄ are shown in Appendix C. We note that

we have not taken into account charge transfer effects explicitly in our model. The mixing of iron and oxygen orbitals gives rise to charge transfer effects in core level spectroscopies. It has been shown that neutral experiments on relatively ionic systems map very accurately to the crystal field multiplet model [refer to de Groot & Kotani (2008) for example]. This is the basis of crystal field theory, where the hybridization is effectively taken care of by the reduction of the Slater integrals from their atomic values, *i.e.* an extra reduction with respect to the 80% reduction of the Hartree–Fock values.

Finally, the magnetic exchange Hamiltonian is given as

$$H_{\text{exch}} = J_{\text{exch}}(n \cdot S), \quad (5)$$

where S is the spin operator, n is a unit vector giving the direction of the magnetization and J_{exch} is the magnitude of the mean-field exchange interaction which we use as 90 meV in our calculation. This value is based on previous $2p3d$ RIXS measurements that showed that the spin-flip excitation is observed at this energy [see, for example, Huang *et al.* (2017) and Elnaggar *et al.* (2019a,b)].

3. Results and discussion

3.1. Construction of the conductivity tensor

The general XAS cross-section can be expressed by equation (6) where ϵ is the polarization vector, Im is the imaginary part of the equation and σ is the conductivity tensor describing the material properties (Haverkort *et al.*, 2010),

$$\text{XAS}^{\text{Dipole}}(\epsilon) \propto -\text{Im}[\epsilon^* \cdot \sigma \cdot \epsilon]. \quad (6)$$

The conductivity tensor is a 3×3 matrix for a dipole transition as shown in equation (7). The matrix elements of the conductivity tensor are defined in equation (8) where ψ is the ground state wavefunction, $T_{x(y)} = \epsilon_{x(y)} \cdot r_{x(y)}$ is the dipole transition operator, H is the Hamiltonian (taking into account the core-hole effect) and γ is the Lorentzian broadening given by the core-hole lifetime [$L_3 = 200$ meV and $L_2 = 500$ meV half width at half-maximum (HWHM) (de Groot, 2005); L_2 has a larger lifetime broadening due to the Coster–Kronig Auger decay],

$$\sigma = \begin{pmatrix} \sigma_{xx} & \sigma_{xy} & \sigma_{xz} \\ \sigma_{yx} & \sigma_{yy} & \sigma_{yz} \\ \sigma_{zx} & \sigma_{zy} & \sigma_{zz} \end{pmatrix}, \quad (7)$$

$$\sigma_{xy} = \left\langle \psi \left| T_y^\dagger \frac{1}{\omega - H + i(\gamma/2)} T_x \right| \psi \right\rangle. \quad (8)$$

In the most general case, nine independent measurements are required to fully reconstruct the conductivity tensor. However, the crystal symmetry can simplify the conductivity tensor by dictating the equivalence between matrix elements or cancelling out some of the matrix elements. For a cubic crystal system with the magnetic field aligned parallel to the high symmetry $[1,0,0]$ direction, only five of the nine matrix elements are non-zero (three diagonal elements: σ_{xx} , σ_{yy} , σ_{zz} ;

Table 1

Experimentally measured XAS spectra and the linear combinations required to construct σ_{xx} , σ_{yy} , σ_{xy} and σ_{yx} matrix elements of the conductivity tensor.

Measured	Constructed
$\epsilon_{\text{LH}} \parallel [1, 0, 0]$	$\sigma_{xx} = \text{XAS}_{\text{LH}}$
$\epsilon_{\text{L30}} \parallel [\sqrt{3}/2, -1/2, 0]$	$\sigma_{yy} = \text{XAS}_{\text{CL}} + \text{XAS}_{\text{CR}} - \text{XAS}_{\text{LH}}$
$\epsilon_{\text{CL}} \parallel [I/\sqrt{2}, -I/\sqrt{2}, 0]$	$\sigma_{xy} = \frac{1}{6}[2\sqrt{3}\text{XAS}_{\text{LH}} - 4\sqrt{3}\text{XAS}_{\text{L30}} + (\sqrt{3} - 3I)\text{XAS}_{\text{CR}} + (\sqrt{3} + 3I)\text{XAS}_{\text{CL}}]$
$\epsilon_{\text{CL}} \parallel [I/\sqrt{2}, I/\sqrt{2}, 0]$	$\sigma_{yx} = \frac{1}{6}[2\sqrt{3}\text{XAS}_{\text{LH}} - 4\sqrt{3}\text{XAS}_{\text{L30}} + (\sqrt{3} + 3I)\text{XAS}_{\text{CR}} + (\sqrt{3} - 3I)\text{XAS}_{\text{CL}}]$

and two off-diagonal elements: σ_{yz} and σ_{zy}). The cubic crystal field implies that the x , y and z directions are equivalent by symmetry; however, if the external magnetic field is aligned to the x axis (and consequently the magnetization), it breaks the equivalency. For this reason, σ_{xx} will be different from σ_{zz} and σ_{yy} . In addition, the magnetization along x induces off-diagonal terms σ_{yz} (σ_{zy}) leading to a scenario where an electric field in the $y(z)$ direction can produce an excitation in the $z(y)$ direction. The off-diagonal terms cannot be directly measured; however, they can be reconstructed from linear combinations of XAS measurements. We first focus on reconstructing the terms σ_{xx} , σ_{yy} , σ_{xy} and σ_{yx} ; hence four independent XAS measurements were performed for this purpose as shown in Table 1.

The response function is a complex quantity and one needs to compute the real part of the function. The real and the imaginary parts of the response function are related to each other through the Kramers–Kronig relation, which allows the computation of the real part from the XAS measurements [see Figs. 1(b) and 1(c)]. Linear combinations of these measurements can now be created according to Table 1 to give the matrix elements of the conductivity tensor. The four matrix elements (σ_{xx} , σ_{yy} , σ_{xy} and σ_{yx}) are shown in Fig. 1(d). One notices that σ_{xx} , σ_{yy} are different which results in a significant XMLD [see Fig. 1(e)]. The off-diagonal terms σ_{xy} and σ_{yx} are about 50 times smaller than the diagonal terms and are roughly equal. These symmetric off-diagonal contributions are possibly due to the presence of small non-cubic distortion in the thin-film. In contrast to the XMLD, the XMCD is negligible as can be seen in Fig. 1(f).

The same procedure can be used to reconstruct the conductivity tensor with the magnetic field aligned to the $[0,0,1]$ direction from four XAS measurements. These matrix elements are shown in Fig. 2. A striking difference can be observed in comparison with Fig. 1(d): the off-diagonal terms σ_{xy} and σ_{yx} are nearly an order of magnitude stronger and are antisymmetric where $\sigma_{xy} \simeq -\sigma_{yx}$. The off-diagonal term differences seen are likely due to small misalignments in the orientation of the magnetization in particular given that the $[0,0,1]$ direction is a magnetically hard direction and does not saturate with 1 T (see Fig. 13 of Appendix A) in combination with the presence of small non-cubic crystal distortion in the thin-film as we showed in earlier work (Elnaggar *et al.*, 2020). The antisymmetric off-diagonal elements result in a

significant XMCD as seen in Fig. 2(c). On the other hand, the XMLD signal is negligible because $\sigma_{xx} \simeq \sigma_{yy}$ [refer to Fig. 2(b)].

The full conductivity tensor can be created by merging together the matrix elements obtained with $B \parallel [1,0,0]$ and $B \parallel [0,0,1]$ as shown in Fig. 3. This procedure assumes that the crystal field is cubic, which is an acceptable assumption given that the off-diagonal matrix elements related to the non-cubic crystal field are very small. With the full conductivity tensor at hand, we can compute XAS for any arbitrary polarization using equation (6). As such, we consider the polarization dependence as it is rotated from $[1,0,0]$ to $[0,1,0]$ in Fig. 4. The computed isotropic XAS and the polarization dependence at $E = 706.4$ eV (red), 707.4 eV (green), 708.4 eV (magenta) and 709.4 eV (blue) are shown in Figs. 4(a) and 4(b), respectively. The measured polarization dependences at these energies are shown in the bottom row of Fig. 4(b) and agree very well with the computation using the full conductivity tensor.

3.2. Magnetic field dependence

The conductivity tensor shown in Fig. 3 gives the response function of the system at a certain magnetic field direction. It is of interest to find the full magneto-optical response of the system as it provides information about the anisotropic magnetic spin-orbit interaction and magnetic moments (van der Laan, 1998; Dhesi *et al.*, 2001, 2002). Symmetry operations of the crystal can be used to relate the conductivity tensor with different magnetic field directions. For example, in a cubic crystal system the conductivity tensors with the magnetic field along x , y and z transform into each other through a 90° rotation. Similar symmetry arguments can be used to relate the conductivity tensor as a function of the magnetic field for different crystal symmetries. Haverkort *et al.* showed that the conductivity tensor can be expressed as a sum of linear independent spectra multiplied by functions depending on the local magnetization direction as given in equation (9) (Haverkort *et al.*, 2010),

$$\sigma(\theta, \phi) = \sum_{k=0}^{\infty} \sum_{m=-k}^k \begin{pmatrix} \sigma_{xx}^{k,m} & \sigma_{xy}^{k,m} & \sigma_{xz}^{k,m} \\ \sigma_{yx}^{k,m} & \sigma_{yy}^{k,m} & \sigma_{yz}^{k,m} \\ \sigma_{zx}^{k,m} & \sigma_{zy}^{k,m} & \sigma_{zz}^{k,m} \end{pmatrix} Y_{k,m}(\theta, \phi). \quad (9)$$

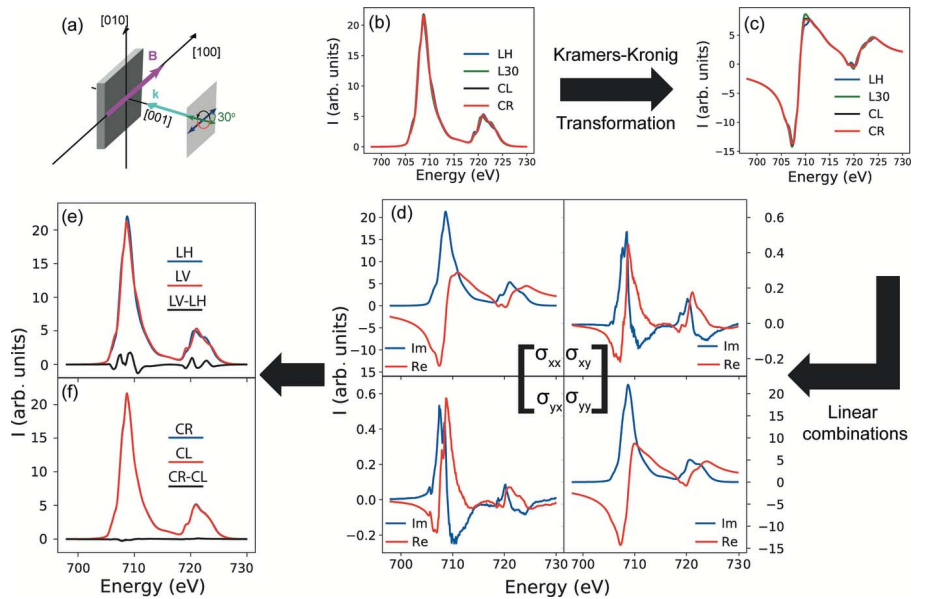


Figure 1 (a) Schematic of the scattering geometry. (b) Fe $L_{2,3}$ XAS measurements in Fe_3O_4 with four linearly independent incident polarizations as described in Table 1 with the magnetic field (B) kept parallel to $[1,0,0]$. (c) The real part of the response function computed by applying a Kramers-Kronig transformation on the XAS measurements in (b). (d) Matrix elements of the conductivity tensor created from linear combinations of the experimental measurements while the XMLD and XMCD measurements are shown in panels (e) and (f), respectively.

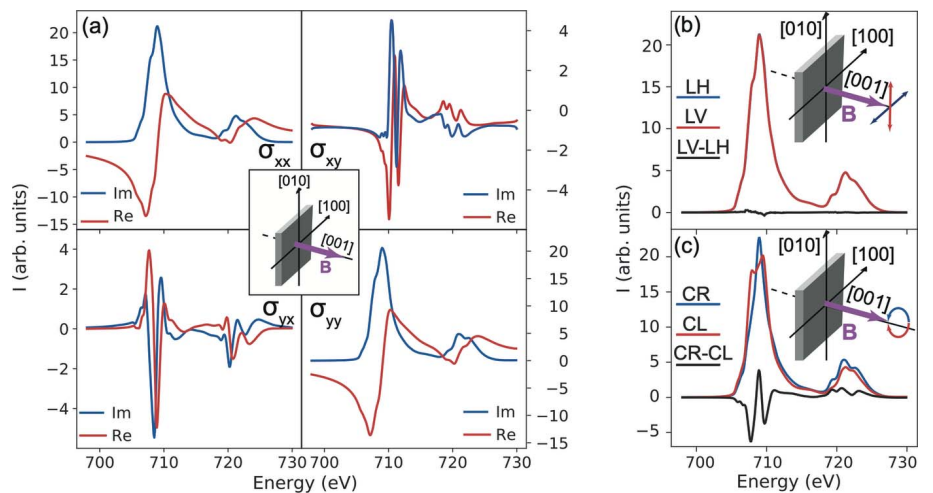


Figure 2 (a) Matrix elements of the conductivity tensor constructed for the Fe $L_{2,3}$ -edge in Fe_3O_4 with $B \parallel [0,0,1]$. The XMLD and XMCD measurements in this configuration are shown in panels (b) and (c), respectively.

Here θ and ϕ define the direction of the local moment with θ being the polar angle, and ϕ being the azimuthal angle. $Y_{k,m}(\theta, \phi)$ is a spherical harmonic function and $\sigma_{i,j}$ is the i,j component of the conductivity tensor on a basis of linear polarized light in the coordinate system of the crystal. This expression allows one to describe the full, magnetic field directional dependent, magneto-optical response of a system by using only a few linear independent fundamental spectral functions. This expression may be simplified for certain crystal systems as we will discuss in the following.

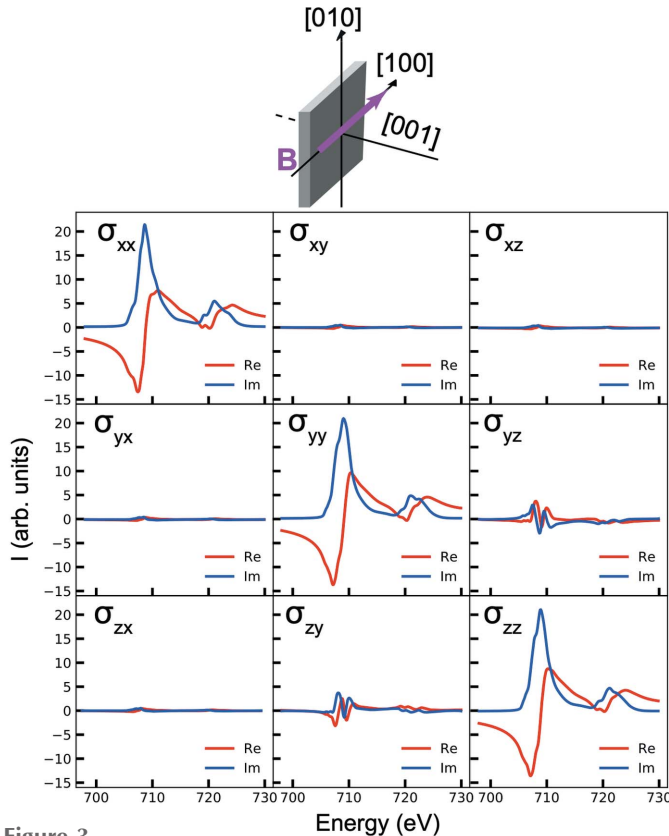


Figure 3
Fe $L_{2,3}$ full conductivity tensor constructed for $B \parallel [1,0,0]$ in Fe_3O_4 .

3.2.1. Spherical field expansion. The crystal field splitting can in some systems be small (in comparison with other interactions such as spin–orbit coupling in rare-earth compounds) and the crystal symmetry can be considered to be nearly spherical. This approximation implies that the spectral shape modification is solely determined by the relative orientation between the magnetization and the polarization. Three fundamental spectra ($\sigma^{(0)}$, $\sigma^{(1)}$ and $\sigma^{(2)}$) connected to the spherical harmonics $Y_{0,0}(\theta, \phi)$, $Y_{1,0}(\theta, \phi)$ and $Y_{2,0}(\theta, \phi)$ are required to describe the conductivity tensor with an arbitrary magnetization direction [equation (10)],

$$\sigma_{[xyz]} = \begin{pmatrix} \sigma^{(0)} + (x^2 - \frac{1}{3})\sigma^{(2)} & -z\sigma^{(1)} + xy\sigma^{(2)} & y\sigma^{(1)} + xz\sigma^{(2)} \\ z\sigma^{(1)} + xy\sigma^{(2)} & \sigma^{(0)} + (y^2 - \frac{1}{3})\sigma^{(2)} & -x\sigma^{(1)} + yz\sigma^{(2)} \\ -y\sigma^{(1)} + xz\sigma^{(2)} & x\sigma^{(1)} + yz\sigma^{(2)} & \sigma^{(0)} + (z^2 - \frac{1}{3})\sigma^{(2)} \end{pmatrix}. \quad (10)$$

The three fundamental spectra of the spherical expansion, $\sigma^{(0)}$, $\sigma^{(1)}$ and $\sigma^{(2)}$, in Fe_3O_4 are shown in Fig. 5(a) and can be used to compute XAS spectra for any orientation of the magnetization. To evaluate the quality of the expansion, we start by comparing the measured and the computed magnetic field angular dependence of XMLD [$I_{\text{XMLD}} = I(\phi) - I(90^\circ)$] with linear horizontal polarization where the magnetic field is rotated from $[1,0,0]$ to $[0,0,1]$ [see Fig. 5(b)]. The expansion reproduces the measured angular dependence well and only

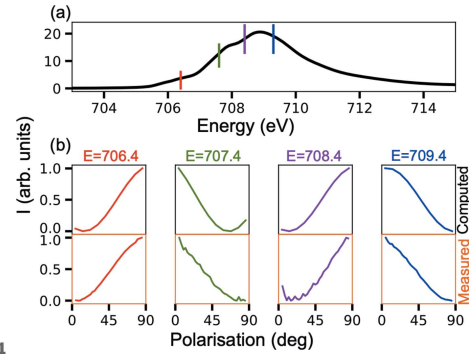


Figure 4
Fe L_3 -edge in Fe_3O_4 . (a) Isotropic XAS constructed from the conductivity tensor. (b) Polarization dependence at $E = 706.4$ eV (red), 707.4 eV (green), 708.4 eV (magenta) and 709.4 eV (blue) where the polarization is rotated from $[1,0,0]$ to $[0,1,0]$. The top row is computed from the conductivity tensor and the bottom row is experimentally measured.

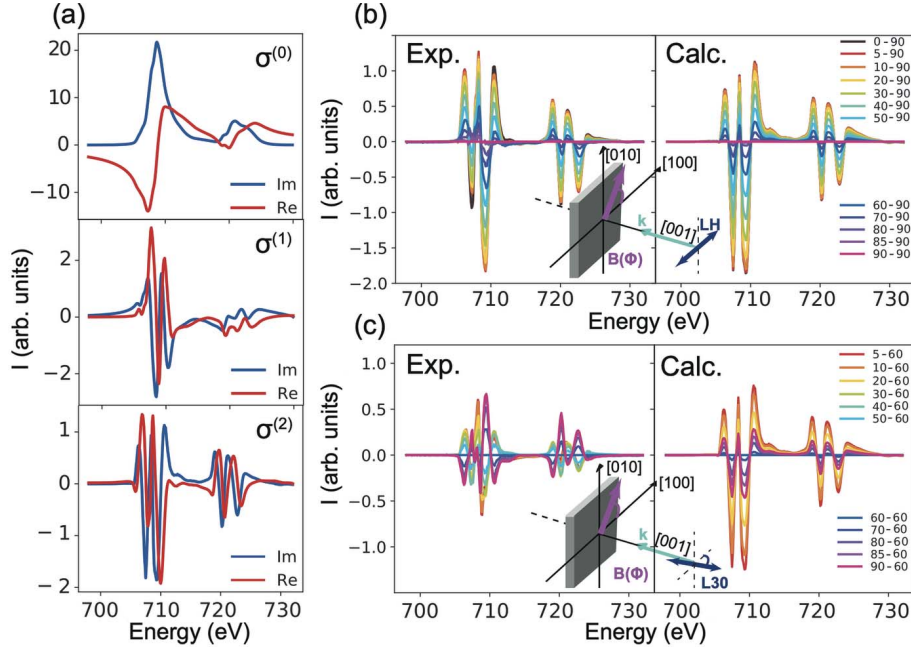
minor discrepancies in the absolute intensities are observed. The angular dependence in this case is given by equation (11) where the two fundamental spectra $\sigma^{(0)}$ and $\sigma^{(2)}$ come into play,

$$I_{\text{LH}}(\phi) = \sigma^{(0)} + \left[\frac{1}{3} - \cos^2(\phi) \right] \sigma^{(2)}. \quad (11)$$

A more interesting case can be observed when the magnetic field angular dependence is measured with the polarization rotated 30° clockwise from the $[1,0,0]$ direction *i.e.* $\epsilon \parallel [\cos(30^\circ), -\sin(30^\circ), 0]$ as shown in Fig. 5(c). Contrary to the results with linear horizontally polarized light, a strong deviation from spherical symmetry is now observed. The expected angular dependence from the spherical field expansion should follow equation (12); however, the spherical field expansion completely breaks down when the polarization is aligned to a low symmetry direction. This is not a surprising result for Fe_3O_4 as its crystal structure is cubic and the crystal field splitting between the t_{2g} and e_g orbitals parametrized through $10D_q$ is ~ 1 eV for Fe in Fe_3O_4 while the spin–orbit coupling is ~ 0.05 eV and the mean field exchange interaction is ~ 0.09 eV. These values suggest that the crystal field cannot be neglected, and a spherical field expansion consequently cannot describe the magneto-optical response of Fe in Fe_3O_4 well,

$$I_{\text{L30}}(\phi) = \sigma^{(0)} + \left[\frac{1}{6} + \frac{\cos(2\phi)}{4} - \frac{\sqrt{3}\sin(2\phi)}{4} \right] \sigma^{(2)}. \quad (12)$$

3.2.2. Cubic field expansion. The local symmetry of the Fe in Fe_3O_4 is nearly cubic (Bragg, 1915), and therefore a more realistic treatment would be to perform a cubic field expansion. In this case, distinctly different measurements can be taken, for example along the fourfold and the threefold symmetry axes, and the fundamental spectra of order k branch according to their symmetry representations in the cubic point group. This is shown in equation (13) where $\sigma^{(2)}$ branches to $\sigma_{e_g}^{(2)}$ for diagonal elements and $\sigma_{t_{2g}}^{(2)}$ for the off-diagonal elements [see Fig. 6(a)]. Furthermore, higher-order k terms such as $\sigma_{t_{1u}}^{(3)}$ become important (Haverkort *et al.*, 2010),


Figure 5

(a) The fundamental spectra $\sigma^{(0)}$, $\sigma^{(1)}$ and $\sigma^{(2)}$ of Fe_3O_4 obtained from a spherical field expansion. (b) Fe $L_{2,3}$ XMLD with linear horizontal polarization (LH) where the XMLD signal is defined as: $\text{XMLD} = \text{XAS}(\phi) - \text{XAS}(90^\circ)$ and ϕ is the angle of the magnetic field. The measured (Exp.) and the calculated (Calc.) result from the spherical field expansion are shown in the left and right panels, respectively. (c) Fe $L_{2,3}$ XMLD measured with linear polarization rotated 30° from the $[1,0,0]$ (labelled L30) where the XMLD signal is defined as: $\text{XMLD} = \text{XAS}(\phi) - \text{XAS}(60^\circ)$.

$$\sigma_{[xyz]} = \begin{pmatrix} \sigma_{a_{1g}}^{(0)} + (x^2 - \frac{1}{3})\sigma_{e_g}^{(2)} & -z\sigma_{t_{1u}}^{(1)} + xy\sigma_{t_{2g}}^{(2)} - z(z^2 - \frac{3}{5})\sigma_{t_{1u}}^{(3)} & y\sigma_{r_{1u}}^{(1)} + xz\sigma_{r_{2g}}^{(2)} + y(y^2 - \frac{3}{5})\sigma_{r_{1u}}^{(3)} \\ z\sigma_{r_{1u}}^{(1)} + xy\sigma_{t_{2g}}^{(2)} + z(z^2 - \frac{3}{5})\sigma_{r_{1u}}^{(3)} & \sigma_{a_{1g}}^{(0)} + (y^2 - \frac{1}{3})\sigma_{e_g}^{(2)} & -x\sigma_{t_{1u}}^{(1)} + yz\sigma_{t_{2g}}^{(2)} - x(x^2 - \frac{3}{5})\sigma_{t_{1u}}^{(3)} \\ -y\sigma_{r_{1u}}^{(1)} + xz\sigma_{t_{2g}}^{(2)} - y(y^2 - \frac{3}{5})\sigma_{r_{1u}}^{(3)} & x\sigma_{r_{1u}}^{(1)} + yz\sigma_{r_{2g}}^{(2)} + x(x^2 - \frac{3}{5})\sigma_{r_{1u}}^{(3)} & \sigma_{a_{1g}}^{(0)} + (z^2 - \frac{1}{3})\sigma_{e_g}^{(2)} \end{pmatrix} \quad (13)$$

A comparison between the measured and computed magnetic field angular dependence of XMLD with linear horizontal polarization can be seen in Fig. 6(b). The agreement between the measurements and the computed field dependence for the spherical and cubic field expansions are of similar quality. The field dependence in this case is given by equation (14) which is of the same form as the spherical field expansion [compare equation (14) with equation (11)] and the fundamental spectra involved are very similar [compare Fig. 6(a) with Fig. 5(a)],

$$I_{\text{LH}}(\phi) = \sigma_{a_{1g}}^{(0)} + \left[\frac{1}{3} - \cos^2(\phi) \right] \sigma_{e_g}^{(2)}. \quad (14)$$

However, contrary to the spherical expansion results, an excellent agreement between the cubic field expansion and the magnetic field angular dependence performed with rotated polarization is now observed in Fig. 6(c). The reason for this improvement is the branching of the $\sigma^{(2)}$ fundamental spectrum into $\sigma_{e_g}^{(2)}$ and $\sigma_{r_{2g}}^{(2)}$ which is probed when the polarization is aligned to a low symmetry direction bringing off-diagonal elements into play. The field dependence for the 30° rotated polarization is given by equation (15) which highlights the role of the $\sigma_{r_{2g}}^{(2)}$ fundamental spectrum. Another important conclusion is that it is essential to measure XAS with the

polarization aligned to a low symmetry direction to sensitively probe the crystal symmetry,

$$I_{\text{L30}}(\phi) = \sigma_{a_{1g}}^{(0)} + \left[\frac{1}{6} + \frac{\cos(2\phi)}{4} \right] \sigma_{e_g}^{(2)} - \left[\frac{\sqrt{3} \sin(2\phi)}{4} \right] \sigma_{r_{2g}}^{(2)}. \quad (15)$$

3.2.3. Convergence of the field expansion. In symmetries lower than spherical, the expansion of the spin (or the magnetic field) direction on spherical harmonics does not truncate at finite k . There is thus, in principle, an infinite number of linearly independent fundamental spectra. Not all of them are important and most of them will be of very low intensity. We have included in our previous analysis terms up to $k = 3$. The cubic field expansion showed a satisfactory agreement with the experimental data and only small discrepancies were showed. Here we investigate theoretically the origin of these discrepancies and the convergence of the field expansion. The quality of an expansion on the spin (or magnetic field direction) is foreseen to depend on the details of the ground state. This is because the magnetization direction depends on both the orbital and spin moments and hence whether the valence orbital moment is quenched or not will affect the efficiency of the expansion. Fe_3O_4 contains both

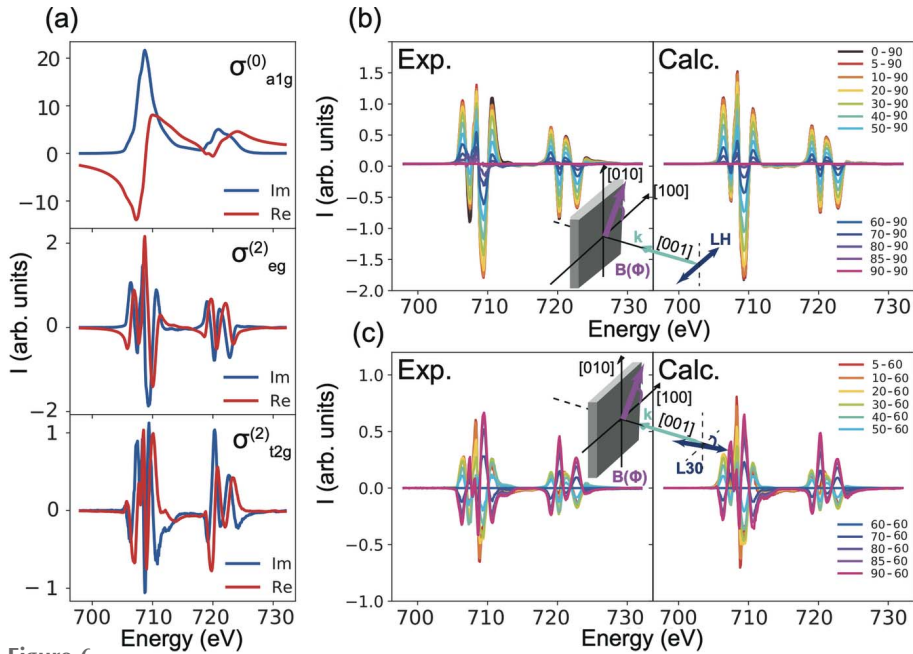


Figure 6 (a) Branching of the fundamental spectra $\sigma^{(0)}$ and $\sigma^{(2)}$ into $\sigma_{a_{1g}}^{(0)}$, $\sigma_{e_g}^{(0)}$ and $\sigma_{t_{2g}}^{(0)}$ of Fe_3O_4 using a cubic expansion. (b) $\text{Fe } L_{2,3}$ XMLD with linear horizontal polarization (labelled LH) where the XMLD signal is defined as: $\text{XMLD} = \text{XAS}(\phi) - \text{XAS}(90^\circ)$ and ϕ is the angle of the magnetic field. The measured (Exp.) and the calculated (Calc.) result from the cubic field expansion are shown in the left and right panels, respectively. (c) $\text{Fe } L_{2,3}$ XMLD measured with linear polarization rotated 30° from the $[1,0,0]$ (labelled L30) where the XMLD signal is defined as $\text{XMLD} = \text{XAS}(\phi) - \text{XAS}(60^\circ)$.

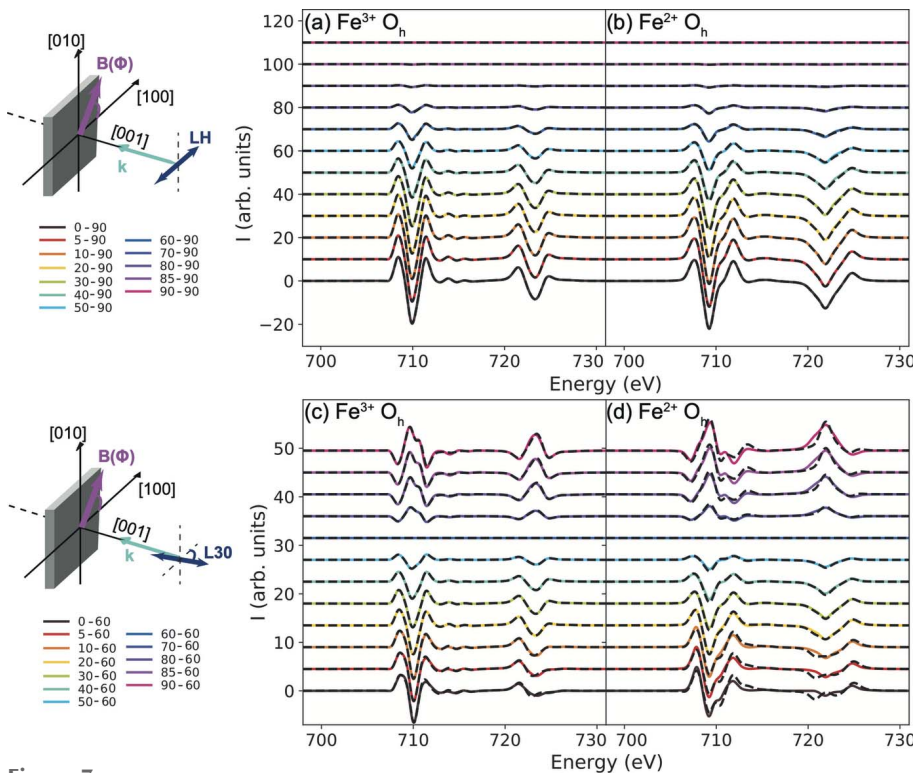


Figure 7 Computed $L_{2,3}$ XMLD: (a) and (b) with linear polarization $\parallel [1,0,0]$ (labelled LH) for Fe^{3+} and Fe^{2+} in O_h symmetry, respectively. The XMLD is defined as: $\text{XMLD} = \text{XAS}(\phi) - \text{XAS}(90^\circ)$ where ϕ is the angle of the magnetic field. The solid lines show XMLD computed individually for every magnetic field orientation while the dashed lines are computed using the cubic field expansion. Panels (c) and (d) are the results with linear polarization rotated 30° from the $[1,0,0]$ (labelled L30) where the XMLD is defined as: $\text{XMLD} = \text{XAS}(\phi) - \text{XAS}(60^\circ)$.

types of ions, Fe^{3+} and Fe^{2+} , providing us with an excellent opportunity to test the effect of the ground state for the two cases. We approach this by calculating the field dependence of XMLD in two ways:

(1) Performing a new full XMLD calculation for every magnetic field orientation.

(2) Computing once the conductivity tensor in equation (13) and then generating the field dependence of XMLD from the cubic fundamental spectra.

The first method is exact and involves no approximations. On the other hand, the accuracy of the second method depends on the order of the expansion used in the calculation. Let us first consider the magnetic field (B) angular dependence probed with the linear polarized X-rays aligned to $[1,0,0]$ where B is rotated about $[0,0,1]$ at $\phi = 0^\circ$. The XMLD signal [computed as $\text{XMLD} = \text{XAS}(\phi) - \text{XAS}(90^\circ)$] for Fe^{3+} and Fe^{2+} in O_h symmetry is shown in Figs. 7(a) and 7(b), respectively. The exact calculations (solid lines) and the cubic field expansion (dashed lines) match well which can initially suggest that the series expanded up to $k = 3$ is sufficient to describe XMLD in $3d$ transition metal oxides. Similar conclusions were reached by Arenholz *et al.* (2006, 2007) and van der Laan *et al.* (2008, 2011). However, a difference between the convergence of the series for both ions can be seen when the polarization is aligned parallel to $[\cos(30^\circ), -\sin(30^\circ), 0]$ [Figs. 7(c) and 7(d)]. Only minor discrepancies are observed for Fe^{3+} while a larger disagreement is observed for Fe^{2+} .

The reason behind the mismatch observed lies in the ground state of Fe^{2+} . In the absence of a magnetic/exchange field, the ground state of the Fe^{2+} ion in O_h symmetry is ${}^5T_{2g}$ composed of 15-fold degenerate states. This degeneracy is split by exchange and spin-orbit interactions leading to a ground state characterized by the spin and orbital momenta projections $s_z = 1.971 (\pm 0.01)$ and $l_z = 0.98 (\pm 0.20)$. On the other hand, the ground state of Fe^{3+} is characterized by the spin and orbital projections $s_z = 2.498 (\pm 0.001)$ and $l_z =$

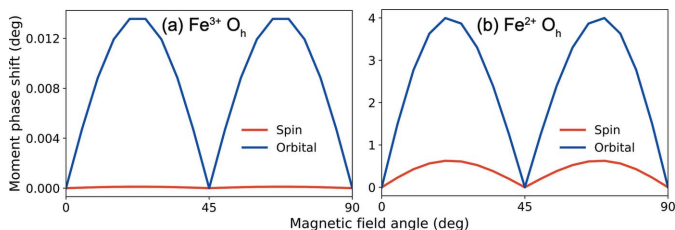


Figure 8
The angle between the spin/orbital (red/blue) moment and the magnetic field as a function of the magnetic field rotation angle for (a) Fe^{3+} in O_h symmetry and (b) Fe^{2+} in O_h symmetry. The magnetic field is rotated about the $[0,0,1]$ starting from the $[1,0,0]$ direction.

0.001 (± 0.001). These values are obtained using the wavefunction calculated by solving equation (1). The reported errors are obtained from the errors in the distortion parameters that are obtained by fitting the XMCD signal using our calculations. We note that the ground state of Fe^{3+} in T_d symmetry is almost identical to that in O_h symmetry and therefore we focus here on the O_h sites (refer to the Appendix C for more details). As the magnetic field is rotated, the spin moment follows the field for the Fe^{3+} as shown in Fig. 8(a). In the case of Fe^{2+} , however, the coupling between the orbital and spin momenta results in a scenario where neither the spin nor the orbital moments follow the rotation of the magnetic field [see Fig. 8(b)] due to the magnetocrystalline anisotropy (Alders *et al.*, 2001). The spin moment can be phase shifted from the direction of the magnetic field with $\sim 0.5^\circ$ while the orbital moment can lag $\sim 4^\circ$ in some directions. This causes the series to converge slower and hence higher orders of k are required. This is further confirmed by the calculation in Fig. 9(a) where the valence spin-orbit coupling is artificially switched off for Fe^{2+} . Now the cubic field expansion repro-

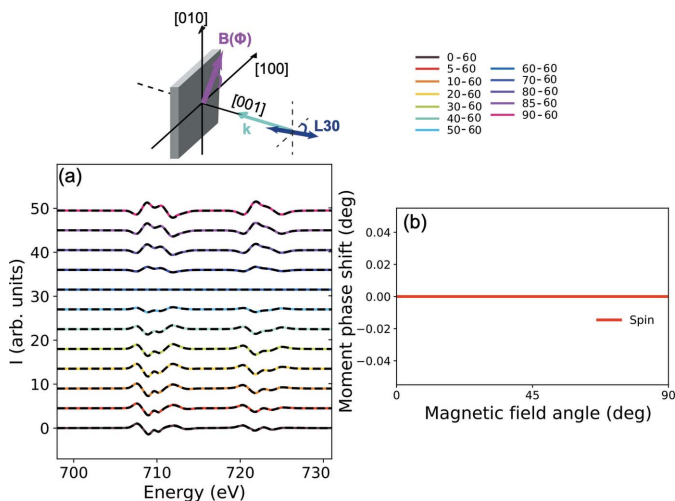


Figure 9
Calculations for Fe^{2+} in O_h symmetry with fully quenched spin-orbit coupling. (a) $L_{2,3}$ XMLD with linear polarization rotated 30° from the $[1,0,0]$ (labelled L30). The XMLD signal is defined as: $\text{XMLD} = \text{XAS}(\phi) - \text{XAS}(60^\circ)$ where ϕ is the angle of the magnetic field. The solid lines show XMLD computed individually for every magnetic field orientation while the dashed lines are computed using the cubic field expansion [equation (15)]. (b) The angle between the spin moment and the magnetic field as a function of the magnetic field rotation angle.

duces the XMLD exquisitely well and no phase shift is observed [Fig. 9(b)].

4. Conclusions

In conclusion, we illustrated the procedure to build the conductivity tensor from experimental measurements which describes the full magneto-optical response of the system. Applied to the Fe $L_{2,3}$ -edge of a 38.85 nm $\text{Fe}_3\text{O}_4/\text{SrTiO}_3$ (001) thin-film, we showed that the convergence of the cubic expansion depends on the details of the ground state. The key aspect that affects the convergence of the expansion in this work is the valence state spin-orbit interaction. While the cubic expansion explains the angular dependence of the XMLD of Fe^{3+} with terms up to the third order, higher-order terms are required for Fe^{2+} . This conclusion is expected to apply for other systems where the valence orbital moments are not quenched.

APPENDIX A Sample characterization

A1. X-ray reflectivity measurement

The Fe_3O_4 (001)/ SrTiO_3 film thickness, interface and surface roughness were examined by X-ray reflectivity using a Philips XPert MRD with Cu K_α radiation (see Fig. 10). The film thickness was concluded to be ~ 38.85 nm. The surface roughness was concluded to be ~ 0.4 nm on average.

A2. Magnetic measurement

Bulk magnetic properties of the Fe_3O_4 (001)/ SrTiO_3 thin-film were investigated using a quantum design dynacool physical properties measurement system. Magnetic moment versus temperature was measured in zero-field cooling mode with 500 Oe applied field [Fig. 11(a)]. A clear peak can be observed at $T = 114.97 \pm 0.29$ K in the derivative signal (the Verwey transition) confirming the good stoichiometry and quality of the thin-film. A comparison between the derivative signal between the thin-film used for this work and a single crystal of the same orientation is shown in Fig. 11(b). The Verwey transition is significantly broader for the thin-film (FWHM = 13.03 ± 0.71 K, centre = 114.97 ± 0.29 K) in

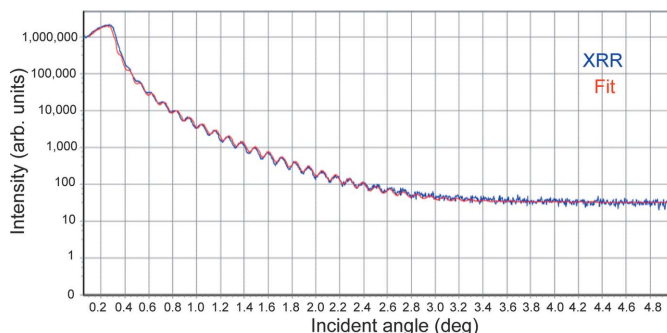


Figure 10
XRR measurement performed on the Fe_3O_4 (001)/ SrTiO_3 thin-film.

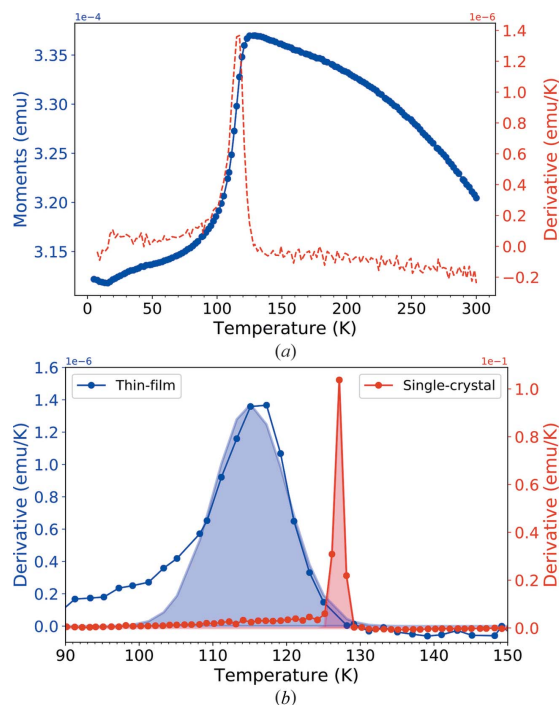


Figure 11
Zero-field cooled magnetization measurement (a) for the Fe_3O_4 (001)/ SrTiO_3 thin-film. (b) Comparison between the derivative of the magnetization measurement for the Fe_3O_4 (001)/ SrTiO_3 thin-film in blue and a single crystal of Fe_3O_4 (001) in red. Gaussian fits of the peaks for two samples are shown in filled colours.

comparison with the single crystal ($\text{FWHM} = 1.40 \pm 0.01$ K, centre = 127.08 ± 0.01 K). This could be related to defects and domain formations in the thin-film which is typical for growth on SrTiO_3 .

Hysteresis loop measurements were also performed along the $[1,0,0]$ axis to inspect the saturation of the film below and above the Verwey transition parallel to the in-plane $[1,0,0]$ direction (Fig. 12). The largest coercivity is observed for the lowest temperature ($H_c = 0.1$ T) and an external magnetic field of 0.25 T is required to saturate the in-plane magnetization. On the contrary, the magnetization is not saturated along the $[0,0,1]$ direction with a field of $H_c = 2$ T as shown by the XMCD signal shown in Fig. 13.

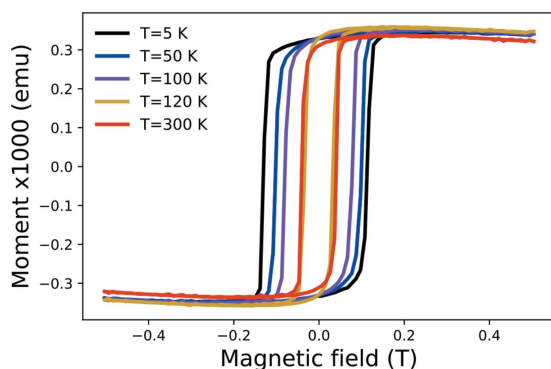


Figure 12
Magnetization loops measurement performed on the Fe_3O_4 (001)/ SrTiO_3 thin-film along the $[1,0,0]$ axis. Five temperatures were investigated, namely $T = 5$ K, 50 K, 100 K, 150 K and 300 K.

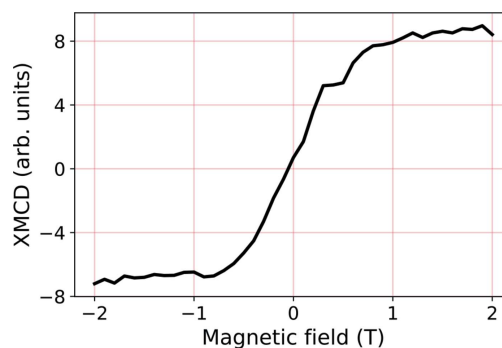


Figure 13
Magnetization of the Fe_3O_4 (001)/ SrTiO_3 thin-film measured at 200 K by recording the intensity of the XMCD at 709.5 eV as a function of the external magnetic field along the $[0,0,1]$ direction.

APPENDIX B Data treatment

In order to compare the XAS results measured at different magnetic field orientations it is necessary to normalize the spectra. The edge jumps (L_3 and L_2) were fitted by two error functions positioned at 708.8 eV and 721.5 eV, respectively [refer to the grey dashed line in Fig. 14(a)]. The multiplet features of the spectra were fitted by a set of Gaussian functions. Six Gaussian functions were used to fit the L_3 part of the spectra [red peaks in Fig. 14(a)] and four to fit the L_2 [blue peaks in Fig. 14(a)]. Only the amplitude of the functions was allowed to float between the data while the energy positions and widths were kept constant between all the data. Table 2 (Table 3) shows the centre and width of the Gaussian peaks used for the L_3 (L_2) edge. We normalized the spectra by setting the L_2 edge jump to unity. The $L_{2,3}$ edge jumps were subtracted from the data as shown in Fig. 14(b). Finally, the spectra were normalized to the spectral area.

APPENDIX C Ground state of Fe ions in Fe_3O_4

C1. Fe^{2+} in octahedral symmetry

The high spin Fe^{2+} ion in octahedral symmetry 15-fold ${}^5T_{2g}$ state [shown in Fig. 15(a)] is split by exchange interaction [90 meV applied according to equation (5)] which lowers the degeneracies leading to a triplet ground state as illustrated in

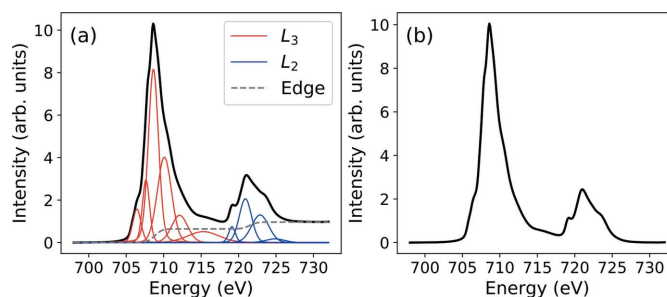


Figure 14
(a) Fitting of the XAS signal of the Fe_3O_4 (001)/ SrTiO_3 thin-film. (b) Background removal.

Table 2
Gaussian peak centre and width used for fitting the L_3 -edge.

Peak	Centre (eV)	HWHM (eV)
1	706.424	0.643
2	707.637	0.561
3	708.631	0.793
4	710.097	1.115
5	712.131	1.252
6	715.302	2.447

Table 3
Gaussian peak centre and width used for fitting the L_2 -edge.

Peak	Centre (eV)	HWHM (eV)
1	719.122	0.527
2	720.908	0.963
3	722.880	1.343
4	724.852	1.422

Fig. 15(b). The spin–orbit coupling finally lifts all the degeneracies as shown in Fig. 15(c). The ground state is 99.8% pure in terms of crystal field configuration and has an occupation $|(t_{2g})^{3.9997}(e_g)^{2.0003}|$ and is 97.21% composed of the state characterized by $m_z = -2$ and $l_z = -1$. We point out that the first and second excited states are ~ 22 and 53 meV higher in energy than the ground state which leads to a Boltzmann occupation of $\sim 75.8\%$, 20.6% and 3.6% of the ground, first and second excited states, respectively, at 200 K. These have been included in the calculation of the spectra. All the parameters used in the multiplet calculations of Fe^{2+} XAS are reported in Table 4.

C2. Fe^{3+} in octahedral and tetrahedral symmetry

The ground states of Fe^{3+} in O_h and T_d symmetries are almost identical with $s_z = 2.499$ and $l_z = 0.001$. Indeed, the 6A_1 splits to the doublet E_2 and quartet G states; however, this splitting can be neglected (the splitting is less than 0.1 meV and is thermally populated). This is illustrated in Figs. 16 and 17 where the ${}^6A_{1(g)}$ state [panel (a)] is split mainly due to exchange interaction [panel (b)] while spin–orbit coupling has

Table 4
Parameters used for the XAS calculation of the $Fe^{2+} O_h$ ion.

Parameter	Initial state (eV)	Final state (eV)	Comment
$10Dq$	1.25	1.25	Similar to the values reported by Patrick <i>et al.</i> (2002) and Arenholz <i>et al.</i> (2006) for Fe_3O_4 . This crystal field parameter reproduces well XAS, XMCD and XMLD measurements in Fe_3O_4 .
F_{dd}^2	7.676	8.245	Atomic Hartree–Fock calculation scaled to 70% to take interatomic screening and mixing. This is in line with the literature such as the work by Patrick <i>et al.</i> (2002) and Arenholz <i>et al.</i> (2006).
F_{dd}^4	4.771	5.129	
F_{pd}^2	–	5.434	Atomic Hartree–Fock calculation scaled to 80%. This is in accordance to the literature such as Patrick <i>et al.</i> (2002) and Arenholz <i>et al.</i> (2006).
G_{pd}^1	–	3.208	
G_{pd}^3	–	2.274	
ξ_d	0.052	0.052	Atomic value which is a reasonable approximation as the spin–orbit coupling is nearly an atomic quantity that is material independent.
ξ_p	–	8.2	
J_{exch}	0.09	0.09	This value is based on previous $2p3d$ RIXS measurements that showed that the spin-flip excitation is observed at this energy [see, for example Huang <i>et al.</i> (2017) and Elnaggar <i>et al.</i> (2019a,b)].
Lifetime broadening (HWHM)	L_3 : 0.2, L_2 : 0.5		The lifetime broadening for the L_3 used is 0.2 eV and for L_2 is 0.5 eV.

negligible effect [panel (c)] for Fe^{3+} in both T_d and O_h symmetries. We point out that the first excited state is ~ 90 meV higher in energy than the ground state which leads to a Boltzmann occupation of $\sim 99.6\%$ and 0.4% of the ground and first excited state, respectively, at 200 K. We therefore only used the ground state in the calculation of the spectra. All the parameters used in the multiplet calculations of $Fe^{3+} O_h$ and T_d XAS are reported in Tables 5 and 6, respectively.

Acknowledgements

We are thankful to R.-P. Wang, M. Ghiasi and M. Delgado for helping with the synchrotron measurements. The synchrotron

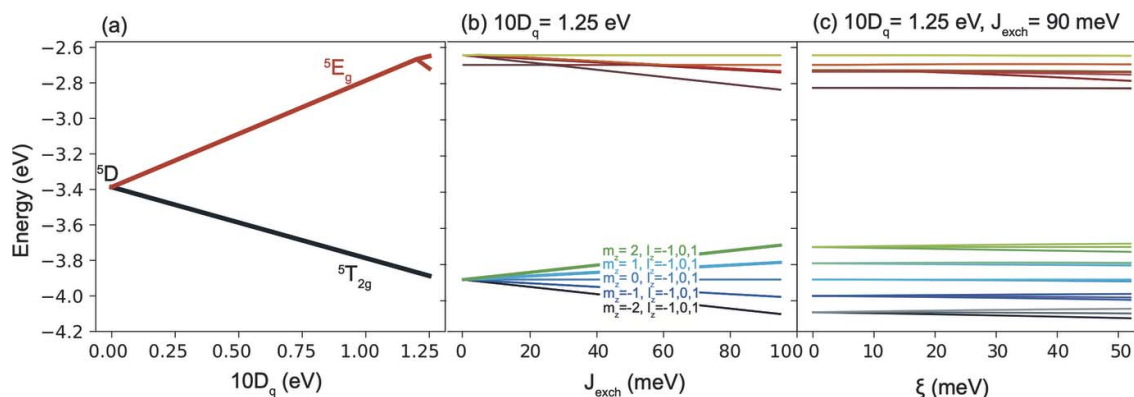
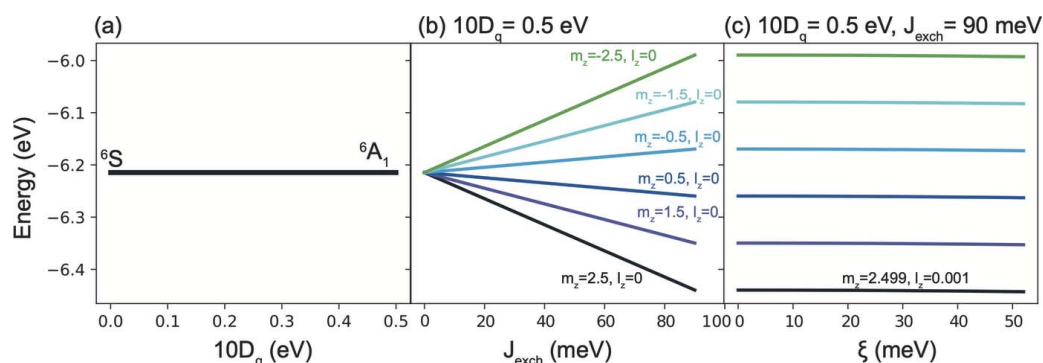
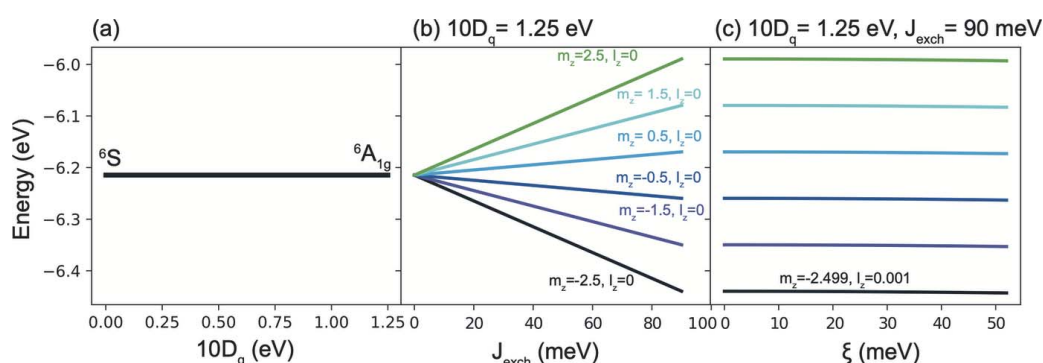


Figure 15
Energy diagrams illustrating the splitting of the ground state of a $d^6 Fe^{2+}$ ion. (a) As a function of the octahedral crystal field $10D_q$ parameter with the spin–orbit coupling (ξ) and magnetic exchange interaction (J_{exch}) set to zero. (b) As a function of J_{exch} with $10D_q = 1.25$ eV and $\xi = 0$. (c) As a function of ξ with $J_{exch} = 90$ meV and $10D_q = 1.25$ eV.


Figure 16

Energy diagrams illustrating the splitting of the ground state of a $d^5 \text{Fe}^{3+}$ ion. (a) As a function of the tetrahedral crystal field $10D_q$ parameter (note that $10D_q T_d = -10D_q O_h$) with the spin-orbit coupling (ξ) and exchange interaction (J_{exch}) set to zero. (b) As a function of J_{exch} with $10D_q = 0.5 \text{ eV}$ and $\xi = 0$. We note that the definition of $J_{\text{exch}} T_d = -J_{\text{exch}} O_h$ because the sites are antiferromagnetically coupled. (c) As a function of ξ with $J_{\text{exch}} = 90 \text{ meV}$ and $10D_q = 0.5 \text{ eV}$.


Figure 17

Energy diagrams illustrating the splitting of the ground state of a $d^5 \text{Fe}^{3+}$ ion. (a) As a function of the octahedral crystal field $10D_q$ parameter with the spin-orbit coupling (ξ) and exchange interaction (J_{exch}) set to zero. (b) As a function of with $10D_q = 1.25 \text{ eV}$ and $\xi = 0$. (c) As a function of ξ with $J_{\text{exch}} = 90 \text{ meV}$ and $10D_q = 1.25 \text{ eV}$.

Table 5

Parameters used for the XAS calculation of the $\text{Fe}^{3+} O_h$ ion.

Parameter	Initial state (eV)	Final state (eV)	Comment
$10D_q$	1.25	1.25	Similar to the values reported by Patrick <i>et al.</i> (2002), Liu <i>et al.</i> (2017) and Arenholz <i>et al.</i> (2006) for Fe_3O_4 . This crystal field parameter reproduces well XAS, XMCD and XMLD measurements in Fe_3O_4 .
F_{dd}^2	8.429	8.972	Atomic Hartree-Fock calculation scaled to 70% to take interatomic screening and mixing. This is in line with the literature such as the work by Patrick <i>et al.</i> (2002) and Arenholz <i>et al.</i> (2006).
F_{dd}^4	5.274	5.616	
F_{pd}^2	–	5.956	Atomic Hartree-Fock calculation scaled to 80%. This is in accordance with the literature such as Patrick <i>et al.</i> (2002) and Arenholz <i>et al.</i> (2006).
G_{pd}^1	–	4.450	
G_{pd}^3	–	2.532	
ξ_d	0.052	0.052	Atomic value which is a reasonable approximation as the spin-orbit coupling is nearly an atomic quantity that is material independent.
ξ_p	–	8.2	
J_{exch}	0.09	0.09	This value is based on previous $2p3d$ RIXS measurements that showed that the spin-flip excitation is observed at this energy [see, for example, Huang <i>et al.</i> (2017) and Elnaggar <i>et al.</i> (2019a,b)].
Lifetime broadening (HWHM).	$L_3: 0.2, L_2: 0.5$		The lifetime broadening for the L_3 used is 0.2 eV and for L_2 is 0.5 eV

experiments were performed at the I06 beamline, Diamond Light Source, UK under proposal number SI-17588. We are grateful for the help of the beamline staff to setup and perform the experiments.

Funding information

The following funding is acknowledged: European Research Council (grant No. 340279 to Frank M. F. de Groot; award No. SI-17588 to Hebatalla Elnaggar).

References

- Alders, D., Coehoorn, R. & de Jonge, W. J. M. (2001). *Phys. Rev. B*, **63**, 054407.
- Alders, D., Tjeng, L. H., Voogt, F. C., Hibma, T., Sawatzky, G. A., Chen, C. T., Vogel, J., Sacchi, M. & Iacobucci, S. (1998). *Phys. Rev. B*, **57**, 11623–11631.
- Arenholz, E., van der Laan, G., Chopdekar, R. V. & Suzuki, Y. (2006). *Phys. Rev. B*, **74**, 094407.
- Arenholz, E., van der Laan, G., Chopdekar, R. V. & Suzuki, Y. (2007). *Phys. Rev. Lett.* **98**, 197201.
- Bragg, W. H. (1915). *Nature*, **95**, 561.
- Carra, P., Thole, B. T., Altarelli, M. & Wang, X. (1993). *Phys. Rev. Lett.* **70**, 694–697.
- Chen, C. T., Tjeng, L. H., Kwo, J., Kao, H. L., Rudolf, P., Sette, F. & Fleming, R. M. (1992). *Phys. Rev. Lett.* **68**, 2543–2546.
- Chen, J. M., Hu, Z., Jeng, H. T., Chin, Y. Y., Lee, J. M., Huang, S. W., Lu, K. T., Chen, C. K., Haw, S. C., Chou, T. L., Lin, H.-J., Shen, C. C.,

Table 6
Parameters used for the XAS calculation of the Fe³⁺ T_d ion.

Parameter	Initial state (eV)	Final state (eV)	Comment
10Dq	−0.5	−0.5	Similar to the values reported by Patrick <i>et al.</i> (2002), Liu <i>et al.</i> (2017) and Arenholz <i>et al.</i> (2006) for Fe ₃ O ₄ . This crystal field parameter reproduces well XAS, XMCD and XMLD measurements in Fe ₃ O ₄ . We note that this is the total crystal field parameter as used in the crystal field multiplet model, <i>i.e.</i> including the effective effects of charge transfer.
F_{dd}^2	8.429	8.972	Atomic Hartree–Fock calculation scaled to 70% to take interatomic screening and mixing. This is in line with the literature such as the work by Patrick <i>et al.</i> (2002) and Arenholz <i>et al.</i> (2006).
F_{dd}^4	5.274	5.616	
F_{pd}^2	–	5.956	Atomic Hartree–Fock calculation scaled to 80%. This is in accordance with the literature such as Patrick <i>et al.</i> (2002) and Arenholz <i>et al.</i> (2006).
G_{pd}^1	–	4.450	
G_{pd}^3	–	2.532	
ξ_d	0.052	0.052	Atomic value which is a reasonable approximation as the spin–orbit coupling is nearly an atomic quantity that is material independent.
ξ_p	–	8.2	
J_{exch}	−0.09	−0.09	This value is based on previous 2p3d RIXS measurements that showed that the spin-flip excitation is observed at this energy [see, for example, Huang <i>et al.</i> (2017); Elnaggar <i>et al.</i> (2019a,b)].
Lifetime broadening (HWHM)	L_3 : 0.2, L_2 : 0.5		The lifetime broadening for the L_3 used is 0.2 eV and for L_2 is 0.5 eV.

Liu, R. S., Tanaka, A., Tjeng, L. H. & Chen, C. T. (2010). *Phys. Rev. B*, **81**, 201102.

Cowan, R. (1981). *The Theory of Atomic Structure and Spectra*. University of California Press.

Csiszar, S. I., Haverkort, M. W., Hu, Z., Tanaka, A., Hsieh, H. H., Lin, H.-J., Chen, C. T., Hibma, T. & Tjeng, L. H. (2005). *Phys. Rev. Lett.* **95**, 187205.

Dhesi, S. S., van der Laan, G. & Dudzik, E. (2002). *Appl. Phys. Lett.* **80**, 1613–1615.

Dhesi, S. S., van der Laan, G., Dudzik, E. & Shick, A. B. (2001). *Phys. Rev. Lett.* **87**, 067201.

Elnaggar, H., Sainctavit, P., Juhin, A., Lafuerza, S., Wilhelm, F., Rogalev, A., Arrio, M.-A., Brouder, C., van der Linden, M., Kakol, Z., Sikora, M., Haverkort, M. W., Glatzel, P. & de Groot, F. M. F. (2019a). *Phys. Rev. Lett.* **123**, 207201.

Elnaggar, H., Wang, R.-P., Ghiasi, M., Yañez, M., Delgado-Jaime, M. U., Hamed, M. H., Juhin, A., Dhesi, S. S. & de Groot, F. (2020). *Phys. Rev. Mater.* **4**, 024415.

Elnaggar, H., Wang, R.-P., Lafuerza, S., Paris, E., Tseng, Y., McNally, D., Komarek, A., Haverkort, M., Sikora, M., Schmitt, T. & de Groot, F. M. F. (2019b). *Appl. Mater. Interfaces*, **11**, 36213–36220.

Finazzi, M., Brambilla, A., Biagioni, P., Graf, J., Gweon, G.-H., Scholl, A., Lanzara, A. & Duò, L. (2006). *Phys. Rev. Lett.* **97**, 097202.

Groot, F. de (2005). *Coord. Chem. Rev.* **249**, 31–63.

Groot, F. M. F. de & Kotani, A. (2008). *Core Level Spectroscopy of Solids*, 1st ed. CRC Press.

Hamed, M. H., Hinz, R. A. L., Lömker, P., Wilhelm, M., Gloskovskii, A., Bencok, P., Schmitz-Antoniak, C., Elnaggar, H., Schneider, C. M. & Müller, M. (2019). *Appl. Mater. Interfaces*, **11**, 7576–7583.

Haverkort, M. W., Csiszar, S. I., Hu, Z., Altieri, S., Tanaka, A., Hsieh, H. H., Lin, H.-J., Chen, C. T., Hibma, T. & Tjeng, L. H. (2004). *Phys. Rev. B*, **69**, 020408.

Haverkort, M. W., Hollmann, N., Krug, I. P. & Tanaka, A. (2010). *Phys. Rev. B*, **82**, 094403.

Haverkort, M. W., Zwierzycki, M. & Andersen, O. K. (2012). *Phys. Rev. B*, **85**, 165113.

Hillebrecht, F. U., Ohldag, H., Weber, N. B., Bethke, C., Mick, U., Weiss, M. & Bahrtdt, J. (2001). *Phys. Rev. Lett.* **86**, 3419–3422.

Huang, H. Y., Chen, Z. Y., Wang, R.-P., de Groot, F. M. F., Wu, W. B., Okamoto, J., Chainani, A., Singh, A., Li, Z.-Y., Zhou, J.-S., Jeng, H.-T., Guo, G. Y., Park, J.-G., Tjeng, L. H., Chen, C. T. & Huang, D. J. (2017). *Nat. Commun.* **8**, 15929.

Iga, F., Tsubota, M., Sawada, M., Huang, H. B., Kura, S., Takemura, M., Yaji, K., Nagira, M., Kimura, A., Jo, T., Takabatake, T., Namatame, H. & Taniguchi, M. (2004). *Phys. Rev. Lett.* **93**, 257207.

Kuiper, P., Searle, B. G., Rudolf, P., Tjeng, L. H. & Chen, C. T. (1993). *Phys. Rev. Lett.* **70**, 1549–1552.

Laan, G. van der (1998). *Phys. Rev. B*, **57**, 5250–5258.

Laan, G. van der (2013). *J. Phys. Conf. Ser.* **430**, 012127.

Laan, G. van der, Arenholz, E., Chopdekar, R. V. & Suzuki, Y. (2008). *Phys. Rev. B*, **77**, 064407.

Laan, G. van der, Telling, N. D., Potenza, A., Dhesi, S. S. & Arenholz, E. (2011). *Phys. Rev. B*, **83**, 064409.

Liu, B., Piamonteze, C., Delgado-Jaime, M. U., Wang, R. P., Heidler, J., Dreiser, J., Chopdekar, R., Nolting, F. & de Groot, F. (2017). *Phys. Rev. B*, **96**, 054446.

Lüning, J., Nolting, F., Scholl, A., Ohldag, H., Seo, J. W., Fompeyrine, J., Locquet, J.-P. & Stöhr, J. (2003). *Phys. Rev. B*, **67**, 214433.

Luo, C., Ryll, H., Back, C. H. & Radu, F. (2019). *Sci. Rep.* **9**, 18169.

Núñez Regueiro, M. D., Altarelli, M. & Chen, C. T. (1995). *Phys. Rev. B*, **51**, 629–631.

Patrick, R. A. D., Van Der Laan, G., Henderson, C. M. B., Kuiper, P., Dudzik, E. & Vaughan, D. J. (2002). *Eur. J. Mineral.* **14**, 1095–1102.

Scholl, A., Stöhr, J., Lüning, J., Seo, J. W., Fompeyrine, J., Siegart, H., Locquet, J.-P., Nolting, F., Anders, S., Fullerton, E. E., Scheinfein, M. R. & Padmore, H. A. (2000). *Science*, **287**, 1014–1016.